Research Square

Preprints are preliminary reports that have not undergone peer review.
They should not be considered conclusive, used to inform clinical practice,
or referenced by the media as validated information.

Multi-scale characterisation of Paperboard Structure and Deformation via Scanning-SAXS and X-ray Tomography

Sahel Ganji
sahel.ganji@solid.lth.se
Lund University
Stephen A. Hall
Lund University
Jonas Engqvist
Lund University
Sara Johansson
Lund University
Johan Tryding
Tetra Pak (Sweden)
Mikael Nygårds
Billerud AB
Anuj Prajapati
MAX IV Laboratory
Kim Nygård
MAX IV Laboratory

Research Article

Keywords:

Posted Date: November 25th, 2026

DOI: https://doi.org/10.21203/rs.3.rs-11610606/v1

License: This work is licensed under a Creative Commons Attribution 4.0 International License.
Read Full License

Additional Declarations: No competing interests reported.

Cellulose manuscript No.
(will be inserted by the editor)

Multi-scale characterisation of Paperboard Structure and Deformation via Scanning-SAXS and X-ray Tomography

Sahel Ganji · Stephen A. Hall · Jonas Engqvist · Sara Johansson · Johan Tryding · Mikael Nygårds · Anuj Prajapati · Kim Nygård

Received: date / Accepted: date

Abstract Scanning small-angle X-ray scattering (scanning SAXS) is combined with high-resolution X-ray microtomography (μXRT) and mechanical testing to investigate paperboard structure and its orthotropic deformation across scales. The presented multi-scale approach links fibril-level structural changes to fibre-network architecture and macroscopic failure, providing insight into the sequence of damage evolution in paperboard. The studied material set includes three-ply boards and individual plies plus isotropic reference sheets of softwood (SW), chemi-thermomechanical pulp (CTMP) and blends of the two.

Before tensile loading, two-dimensional (2D) SAXS mapping revealed clear nanostructural differences between the fibre types. Softwood-rich materials showed a more dominant cellulose fibril correlation peak, whereas CTMP-containing materials exhibited additional features at low scattering-vector magnitudes (q), indicating a more heterogeneous fibre-wall structure.

During stepwise tensile loading, increased SAXS intensities in the power-law regime are interpreted as the development of internal interfaces, voids and nanoscale damage within the fibre network. These higher intensities in the power-law regime are seen to be localised in the 2D maps over regions around the final fracture, but appear before the fracture. Observed intensity reduction at higher q within the fracture zone suggests that this region contains less ordered fibrillar material. In the three-ply board, combined SAXS and μXRT results suggest a layered damage process, with fracture patterns depending on the loading direction and local fibre composition.

Keywords Paperboard · SAXS · X-ray tomography · μXRT · X-ray scattering · Multi-scale characterisation

S. Ganji (✉) · S. Hall · J. Engqvist · J. Tryding
Division of Solid Mechanics, Department of Construction Sciences, Lund University, Ole Römers Väg 1, 221 00 Lund, Sweden
e-mail: sahel.ganji@solid.lth.se

S. Johansson
Division of Engineering Geology, Department of Biomedical Engineering, Lund University, Ole Römers Väg 1, 221 00 Lund, Sweden

J. Tryding
Tetra Pak AB, Ruben Rausings gata 11A, 223 55 Lund, Sweden

M. Nygårds
Billerud AB, Evenemangsgatan 17, 169 79 Solna, Sweden

A. Prajapati · K. Nygård
MAX IV Laboratory, Lund University, 221 00 Lund, Sweden

Introduction

Paper-based packaging materials, particularly paperboard, are central to ongoing efforts toward more sustainable and circular packaging systems. As concerns over plastic pollution and carbon emissions increase, cellulose-based materials offer clear advantages: they are renewable, biodegradable and widely recyclable. In addition to these environmental benefits, paperboards provide a useful balance of strength, stiffness, formability and printability, making them suitable for protecting products and enabling high-quality surface finishing in a wide range of applications (Hubbe 2014). The push toward lighter, stronger and more resource-efficient packaging has, nevertheless, placed new demands on the mechanical performance of paperboard. During manufacture, converting, distribution and end use, the material is subjected to combinations of tensile, compressive, bending and shear loads. These varied loading conditions can expose limitations in current designs, particularly as basis weights are reduced to meet sustainability targets. Ensuring reliability under these conditions requires not only incremental material development, but also a deeper understanding of how the internal structure at multiple scales governs mechanical behaviour.

The mechanical response of paperboard arises from a hierarchical architecture that spans multiple length scales: nanostructured cellulose fibrils within the fibre wall, fibre–fibre bonds, the meso-scale fibre network and the macroscopic multi-ply construction. Understanding how these structural levels interact and evolve during mechanical loading is essential for optimising material design, refining predictive models and developing more sustainable high-performance packaging materials (Dias et al. 2023).

At the network scale, X-ray microtomography (μXRT) has previously enabled non-destructive three-dimensional (3D) mapping of fibre orientation, density and bonding patterns in paper and paperboard. Such measurements provide quantitative descriptors, such as orientation tensors, for numerical modelling (e.g., Kloppenburg et al. 2024). μXRT-based analyses also reveal structural anisotropies introduced during manufacturing and by the types and proportions of fibres used. These structural variations are known to directly influence stiffness, strength and formability (e.g., Dias et al. 2023; Fellers 2009; Wahlström 2013).

At the scale of individual fibres, optical and electron microscopy together with mechanical testing have been used to quantify fibre geometry, deformation and failure mechanisms. Atomic force microscopy-based force mapping and nanoindentation provide local mechanical characterisation of single cellulose fibres (e.g., Auernhammer et al. 2022), while tensile testing has been used to measure stiffness and strength distributions for different pulps (e.g., El-Hosseiny and Page 1975; Groom et al. 2002; Kompella and Lambros 2002). At the network scale, the load-bearing capacity depends strongly on interfibre bonding and fibre segment activation, while factors such as beating, drying stress and fines content strongly influence bond strength (Vainio and Paulapuro 2007). Together, these previous studies have shown that sheet-level mechanical properties are governed by fibre morphology, bonding area and the microfibril architecture of the cell wall (Barnett and Bonham 2004; Lichtenegger et al. 1999).

At the nanoscale, small-angle X-ray scattering (SAXS) is a well-established tool for probing the hierarchical organisation of cellulose fibrils within the fibre wall. SAXS has been widely used to determine the dimensions of elementary cellulose fibrils and their aggregated structures (e.g., Jakob et al. 1994; Donaldson 2008; Fernandes et al. 2011; Larsson et al. 2022). These studies demonstrate that fibril dimensions and packing vary with pulping method, drying history and sample treatment. Hydration further modifies the scattering response, revealing swelling-dependent changes in interfibrillar spacing (Jakob et al. 1996; 1995) and pore structure in pulp fibres (Larsson et al. 2022). Chemical extractions, likewise, show how removing lignin and hemicellulose alters the matrix surrounding the fibrils and promotes changes in their packing (Jungnikl et al. 2008).

Cellulose microfibril orientation plays a key role in plant cell wall mechanics and influences cell shape during growth. Measurement of microfibril orientation using SAXS is well established for secondary cell walls (Wardrop 1952; Jakob et al. 1994). In these walls, cellulose microfibrils in the S2 layer are predominantly aligned relative to the fibre axis, whereas the S1 and S3 layers contain microfibrils with different and more variable orientations. These differences in microfibril arrangement give rise to characteristic azimuthal distributions in SAXS patterns (Jakob et al. 1994). The orientation of cellulose microfibrils, commonly expressed as the microfibril angle, is a key determinant of fibre stiffness, extensibility and shrinkage. SAXS studies have shown that the microfibril angle varies both within and between fibres (e.g., Barnett and Bonham 2004; Reiterer et al. 1998; Cave 1997) and plays an important role in mechanical optimisation strategies across different species (Lichtenegger et al. 1999). Scanning SAXS, first demonstrated in laboratory setups (Fratzl et al. 1997), has been further developed through synchrotron microbeam techniques that enable high-resolution mapping of fibril orientation and heterogeneity at the cell

wall scale and at the fibre-based material scale (e.g., Saxe et al. 2014; Virtanen et al. 2015; Thomas et al. 2021). These approaches reveal local structural variations, including differences between primary and secondary cell wall layers (Saxe et al. 2014), gradients across growth rings or ply layers (Virtanen et al. 2015) and nanoscale deformation mechanisms under applied loads (Thomas et al. 2021). Together, this existing body of work has established SAXS as a powerful tool for linking fibril-level organisation to fibre mechanics.

Although μXRT, X-ray scattering and mechanical testing have each provided important insights into the structure–property relationships of fibre-based materials, their combined use within a single study remains relatively limited. For example μXRT has been used to visualise fibre- and ply-level architecture and damage mechanisms (e.g., Johansson et al. 2021), X-ray scattering has been applied to determine fibril dimensions and orientation distributions (e.g., Jakob et al. 1995; Fernandes et al. 2011) and mechanical tests have been used to quantify the stiffness and strength of individual fibres (e.g., Page et al. 1977; Groom et al. 2002). However, systematic approaches that combine these techniques on the same fibre-based samples remain rare. Furthermore, most X-ray scattering studies have not tracked the structural evolution of paper or paperboard in-situ during controlled mechanical loading. Many experiments have focused instead on isolated cellulose fibres, wood sections or nanocellulose model systems (e.g., Jakob et al. 1995; Fernandes et al. 2011; Thomas et al. 2021), rather than on intact fibre-based sheets representative of end-use materials. Furthermore, conventional SAXS measurements often average over large heterogeneous regions, which obscures where nanoscale structural changes localise and how they propagate. These limitations hinder our ability to link nanoscale fibril deformation and fibre-bond activation to macroscopic failure mechanisms such as fibre rupture, pull-out or ply delamination. Bridging these scales is essential for advancing fundamental fibre science and guiding the design of stronger and more formable paperboards.

In this study, we address the gaps outlined above using a multi-scale experimental approach. The study material set includes commercial-like three-ply boards, individual ply sheets and isotropic reference sheets. The experimental design combines scanning SAXS to characterise nanostructure and heterogeneity spatially across the samples, stepwise loading in-situ with scanning SAXS mapping to capture the spatio-temporal nanoscale structural evolution during tensile deformation and high-resolution post-mortem μXRT to correlate scattering features with fibre-network architecture.

Materials & Methods

Sample preparation

Three types of samples were prepared: (i) three-ply paperboard structures designed to mimic simplified commercial packaging boards; (ii) single-ply sheets corresponding to each ply in the three-ply structure (top, middle, bottom); (iii) isotropic single-ply sheets made from pure softwood (SW), pure chemi-thermomechanical pulp (CTMP) and a 50:50 SW–CTMP blend. The orthotropic sheets were produced using a dynamic sheet former, while the isotropic sheets were produced using a Rapid-Köthen sheet former, following ISO 5269-2 by Billerud AB. The pulps were collected directly from a Billerud paperboard production line after the refining stage. The softwood kraft pulp and CTMP were characterised using an ABB Lorentzen & Wettre FiberTester, yielding an average fibre length of 2.10 mm and a width of 29.4 µm for the SW fibres and an average fibre length of 1.97 mm and a width of 37.5 µm for the CTMP fibres.

The two main pulp types, SW and CTMP, differ in lignin content, fibre surface chemistry and mechanical behaviour. In the CTMP process, the combination of mechanical energy and mild chemical treatment loosens the lignin matrix, enabling fibre separation while leaving a thin lignin-rich film on the fibre surface. This coating contributes to increased stiffness and influences bonding and deformation behaviour. In contrast, kraft pulping removes most lignin, producing more flexible and conformable SW fibres with higher bonding potential. These differences are expected to affect both the mechanical properties and the small-angle scattering response.

Three-ply board structures were formed by sequential deposition in the dynamic sheet former. The bottom-ply furnish was sprayed first onto the moving wire, followed by the middle ply and finally the top ply, produc-

Table 1 Specifications of the investigated paperboard sheets, including fibre composition, grammage, thickness, strength ratio (MD/CD) and density.

Sample	Fibre composition	Grammage (g/m^2)	Thickness (μm)	Strength ratio (MD/CD)	Density (kg/m^3)
Top ply	SW	129	170	2.2	759
Middle ply	SW–CTMP blend	112	272	1.6	412
Bottom ply	SW	128	172	1.4	744
Three-ply	SW–CTMP blend	270	443	1.2	609

ing an integrated three-layer sheet. After formation, the wet sheets were pressed using a nip and felts, followed by restrained drying to maintain geometry and fibre orientation. The top ply, made entirely of bleached SW fibres, exhibited a machine- to cross-direction (MD/CD) strength ratio of 2.2, provided surface strength and stiffness for the laminate. The middle ply, composed of a 50:50 blend of bleached SW and CTMP, had an MD/CD strength ratio of 1.6 and served as the bulk, more formable layer. The bottom ply, also made from 100 % bleached SW, had an MD/CD strength ratio of 1.4 and provided structural reinforcement. Single-ply sheets with matching fibre compositions were also produced to allow layer-specific comparison. Sample grammage, structural thickness measured according to SCAN-P 88:01, MD/CD strength ratio and density are summarised in Table 1.

To complement the anisotropic, commercial-type sheets, isotropic reference sheets were produced using pure SW (82 g/m^2), pure CTMP (63 g/m^2) and a 50:50 SW–CTMP blend (64 g/m^2). These isotropic samples were included to assess fibre-type effects independent of orientation. The complete sample set provides a simplified but representative model system for multi-scale analysis of fibre-based packaging materials, intentionally excluding coatings or chemical additives.

For tensile testing and X-ray scattering, specimens were prepared with the geometry shown in Fig. 1 in both MD and CD using the laser cutting option on a Snapmaker Artisan system to ensure repeatable notch geometry and minimal edge damage. The notched geometry aimed to focus the deformation and guide failure/crack initiation to a defined region within the intended field of view of the SAXS mapping. Sample dimensions and the scanned area are illustrated in Fig. 1.

SAXS measurements

All SAXS measurements were conducted at the ForMAX beamline of the MAX IV Laboratory, Lund, Sweden (Nygård et al. 2024). 2D raster scanning was employed to map the spatial variations in nanoscale structural features in the samples before loading and during in-situ tensile loading. The X-ray energy was 23.78 keV and the sample-to-detector distance was 3.53 m. Scattering patterns were recorded using a Dectris EIGER2 X 4M detector. The incoming X-ray beam had a rectangular cross section of approximately $91 \times 95\,\mu m^2$. For all the measurements, samples were mounted on a custom-built uniaxial tensile loading device. The device was positioned on the beamline's motorised stage to enable precise alignment and scanning. For the non-deformed

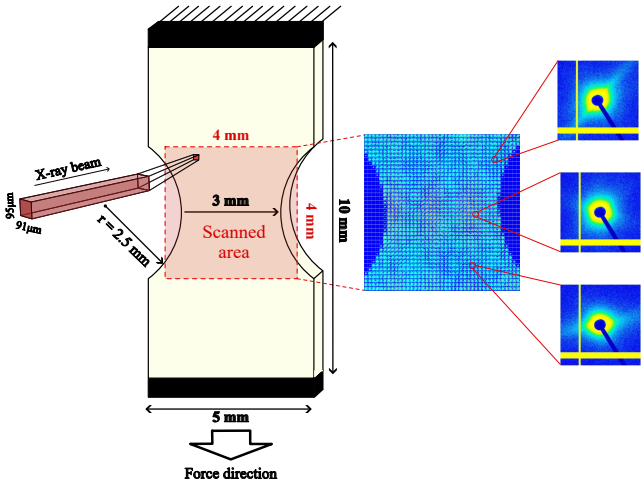

Fig. 1 Specimen geometry and SAXS mesh scanning setup used for the tensile loading configurations. The dotted square indicates the 4 × 4 mm^2 SAXS scanning area, which was mapped using a 95 × 91 µm^2 X-ray beam over a 40 × 41 grid. Example 2D SAXS patterns from selected scan positions are shown on the right.

scans the loading set-up was only used as a stable support for the samples. More information about the in-situ loading is presented in a later section. All the measurements were performed under ambient conditions at the beamline (approximately 24 °C and 40 % relative humidity).

For each SAXS map, a $4 \times 4\,mm^2$ region centred in the gauge area was scanned using a 40×41 grid, yielding 1640 individual SAXS measurements per map. The exposure time was 0.25 s per frame. Raw 2D SAXS images were processed using a custom Python workflow based on the MAX IV processing script using the azint Python package (Jensen et al. 2022) and adapted for the present experiment. To correct for beam-intensity fluctuations, each frame was normalised by its corresponding beamstop monitor signal. Background correction was performed by averaging SAXS frames collected outside the sample region; the associated beamstop monitor signals were also averaged and used to normalise the background before subtraction. The corrected frames were azimuthally integrated using the AzimuthalIntegrator class of the azint Python package (Jensen et al. 2022). Detector geometry was defined from the SAXS .poni calibration file provided by the beamline and invalid pixels were excluded using the corresponding detector mask. The azimuthal integration was used to convert the detector images into intensity distributions as functions of the scattering vector magnitude, q, and azimuthal angle, ϕ, where

$$q = \frac{4\pi}{\lambda} \sin\theta, \tag{1}$$

with the scattering angle 2θ and the X-ray wavelength λ. The data were binned into 1000 radial and 120 azimuthal intervals for subsequent analysis. After SAXS data collection, all samples were carefully dismounted and stored for subsequent X-ray microtomography to correlate nanoscale scattering features with the fibre-network architecture.

SAXS profile fitting and nanostructure characterisation

To compare the nanostructure of paperboard samples produced using different pulping methods, SAXS intensities were averaged over the frames located well inside the scanned area of the samples to improve the signal-to-noise ratio and minimise edge effects. The corresponding 2D SAXS patterns were azimuthally averaged over the full angular range (0°–360°) to obtain one-dimensional (1D) radial intensity profiles representative of the bulk nanostructure for each material type.

These 1D SAXS profiles for each sample type were modelled using a combination of a power-law function and one or two Gaussian peaks, depending on the fibre composition of the sample. For samples composed entirely of SW fibres, $I(q)$, was fitted using a power-law term and a single Gaussian function centred around $q = 0.09$–$0.10\,\text{Å}^{-1}$,

$$I(q) = Pq^{-n} + G_2 \exp\left[-\frac{(q-\mu_2)^2}{2\sigma_2^2}\right], \tag{2}$$

where Pq^{-n} describes the power-law representing large-scale inhomogeneities and the Gaussian term represents a dominant nanostructural correlation length. The fitting parameters are the power-law prefactor P, exponent n, peak amplitude G_2, peak position μ_2 and peak width σ_2.

For samples containing both SW and CTMP fibre types a second Gaussian term was required to capture an additional scattering feature. These intensity profiles were, therefore, modelled using a power-law background and two Gaussian peaks,

$$\begin{aligned} I(q) = Pq^{-n} &+ G_1 \exp\left[-\frac{(q-\mu_1)^2}{2\sigma_1^2}\right] \\ &+ G_2 \exp\left[-\frac{(q-\mu_2)^2}{2\sigma_2^2}\right]. \end{aligned} \tag{3}$$

In these cases, the first Gaussian typically appears at lower q values (around $0.035\,\text{Å}^{-1}$) with the peak amplitude of G_1, while the second peak coincides with the SW-related feature near $0.10\,\text{Å}^{-1}$. By including a second Gaussian peak, three additional fitting parameters were introduced, G_1, μ_1 and σ_1. An example of this fitting for the middle ply is shown in Fig. 2, where the total model is decomposed into its individual components: the power-law representing large-scale structural heterogeneities and the two Gaussian peaks representing the distinct structural correlations.

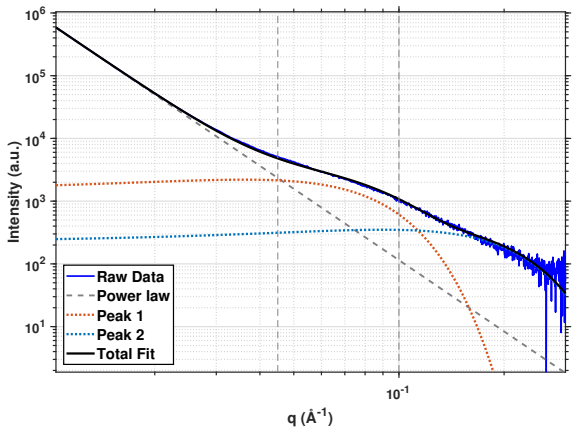

Fig. 2 Example SAXS profile fit for the middle ply. The raw azimuthally averaged data (blue) are fitted using a power-law background (grey dashed) and two Gaussian peaks (red and blue dotted). The total fitted model is shown in black.

The 1D SAXS curve fitting was performed over the range $q = 0.01$ to $0.25\,\text{Å}^{-1}$, selected to capture the relevant structural features while avoiding regions influenced by beamstop artefacts and low signal-to-noise at high q. A custom MATLAB(R) (The MathWorks Inc. 2022) script using nonlinear least-squares optimisation (lsqnonlin) was used for all fits, with initial parameter values and bounds manually tuned to ensure stable convergence across samples. The fitted models for all investigated samples are shown in Fig. 3, allowing direct comparison of the scattering behaviour across fibre types and ply configurations. The vertical dashed markers in Fig. 3 divide the fitted curves into three q-ranges, denoted A, B and C, corresponding, respectively, to the power-law regime, the CTMP-related peak range and the SW-related peak range. These labels are used throughout the following sections for consistency and ease of reference.

Uncertainties for all fit parameters were estimated using bootstrap resampling. For each sample, 500 synthetic intensity profiles were generated by resampling the residuals of the original fit and each synthetic profile was refitted using the same model. The 95 % confidence intervals were then obtained from the resulting parameter distributions.

In some cases, particularly for the higher-q peak, the bootstrap confidence intervals collapsed to values near the lower parameter bounds. The position of this peak was consistently estimated around $0.1\,\text{Å}^{-1}$, but

Table 2 Fitted parameters from SAXS profile analysis for paperboard plies and reference samples. Values in parentheses indicate 95% confidence intervals (CI) from bootstrap resampling.

Sample	$P \times 10^{-2}$	n	G_1	μ_1 (Å^{-1}) [CI]	σ_1 (Å^{-1}) [CI]	G_2	μ_2 (Å^{-1}) [CI]	σ_2 (Å^{-1}) [CI]
SW	1.568 (1.501–1.603)	3.671 (3.666–3.682)	–	–	–	170.9	0.090 (0.088–0.103)	0.099 (0.086–0.103)
CTMP	1.158 (1.000–1.304)	3.777 (3.751–3.811)	2140	0.032 (0.030–0.039)	0.035 (0.030–0.036)	220	0.095 (0.095–0.095)	0.080 (0.080–0.080)
Top	1.743 (1.625–1.804)	3.720 (3.712–3.736)	–	–	–	288.5	0.088 (0.088–0.088)	0.091 (0.089–0.093)
Bottom	1.603 (1.534–1.648)	3.740 (3.734–3.751)	–	–	–	287.8	0.095 (0.088–0.102)	0.086 (0.080–0.094)
Middle	1.841 (1.810–1.886)	3.785 (3.780–3.789)	2515	0.034 (0.033–0.038)	0.036 (0.033–0.038)	405	0.096 (0.096–0.100)	0.087 (0.087–0.102)
Three-ply	4.364 (4.003–4.716)	3.746 (3.729–3.766)	3221	0.030 (0.030–0.038)	0.039 (0.035–0.040)	580	0.118 (0.112–0.120)	0.092 (0.090–0.099)

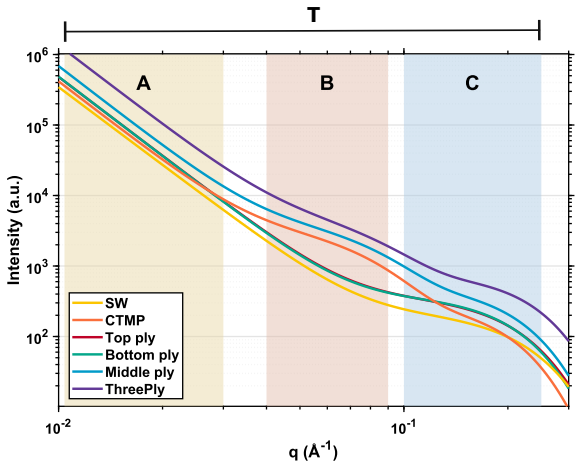

Fig. 3 Comparison of fitted SAXS models for all investigated samples. The curves illustrate how the fitted power-law behaviour and peak structure vary across fibre types and ply configurations. A, B and C indicate the q-ranges used for SAXS mapping, while T denotes the total q-range.

the narrow confidence intervals likely reflect the limited sensitivity of the fit in this region, due to the low peak intensity. As a result, the peak position is only weakly constrained by the data and its bounds for the fitting were kept deliberately narrow based on prior expectations. The fitted parameters for all samples are summarised in Table 2.

Analysis of sample heterogeneity from 2D SAXS mapping

To investigate spatial heterogeneity in the nanostructure of the fibre networks, each point of each SAXS map was analysed, providing spatially resolved scattering information across the scanned area (Fig. 1). Three distinct q-intervals were defined to reflect the underlying structural organisation at different length scales. These intervals correspond to the three q-ranges denoted A, B and C in Fig. 3, which were identified based on the fitted SAXS models, with the corresponding peak positions and widths summarised in Table 2. Q-range A, spanning $q = 0.01$–$0.03\,\text{Å}^{-1}$, captures large-scale heterogeneities and long-range correlations within the fibre network and is dominated by the power-law scattering behaviour. Q-range B, covering $q = 0.04$–$0.09\,\text{Å}^{-1}$, corresponds to the first broad scattering feature predominantly observed in CTMP-containing samples. Q-range C, defined over $q = 0.10$–$0.25\,\text{Å}^{-1}$, corresponds to the tail region of the second Gaussian peak and is typically associated with more compact and aligned fibril structures in softwood (SW) fibres. These intervals were not centred on the peak maxima but instead selected from the trailing edge of each peak, where signal contributions remained strong while interference from overlapping features was minimised. Pixel-wise fitting of the full SAXS profiles was not performed because the signal-to-noise ratio of individual mesh-point patterns was insufficient for stable multi-parameter fitting; therefore, intensity integration over predefined q-ranges was used as a more robust approach. In addition to the individual ranges A–C, an integration was performed over the full q-range to capture total scattering intensity and provide a general overview of nanostructural contrast.

To estimate and remove the power-law background and isolate the peak signals, the azimuthally averaged SAXS intensity was modelled in the low-q range (0.01–$0.03\,\text{Å}^{-1}$), where the contribution from structural peaks is minimal, using a simple power-law function of the form Pq^{-n}. The parameters P and n were obtained through nonlinear least-squares fitting of the mean intensity across this range. This fitted background was then extrapolated over the full q-range of each frame and subtracted pointwise from the corresponding 2D SAXS data to obtain a corrected intensity profile. By removing this estimated contribution from large-scale density inhomogeneities, the procedure enhances the visibility of nanostructural features and allows more robust integration and comparison of intensity within the defined q-ranges.

For each 2D SAXS frame, the scattering intensity was integrated over the selected q-ranges to yield scalar values representing the local scattering response at each beam position. For each q-range, the minimum and maximum intensity values across the entire mesh were used to define the corresponding colour scale. Each scalar intensity was then mapped to one of 30 discrete levels using a customised Viridis colour map. This perceptually uniform colour scale enabled consistent and intuitive visualisation of scattering intensity, where darker purple tones indicated lower values and brighter yellow tones

represented stronger scattering signals. The resulting intensity values were rendered as 300×300 pixel colour tiles and assembled into their original scan layout to reconstruct 2D spatial maps for each q-range.

The maps resulting from the procedure described above reveal clear spatial variations in scattering intensity that depend on the selected q-range, reflecting different underlying structural features. As an illustration, Fig. 4 shows SAXS intensity maps for the middle ply sample in the machine direction across different q-ranges. These differences demonstrate that the combination of spatially resolved SAXS mapping and targeted q-intervals enables differentiation between fibre types and structural organisation within the sheet. In the low-q range (A), the intensity distribution appears relatively smooth and continuous, consistent with large-scale density variations and fibre-network heterogeneity. In contrast, the intermediate-q range (B), associated with CTMP-related nano-structural features, exhibits more localised regions of enhanced intensity, suggesting spatially confined domains where CTMP fibres or fibril bundles are concentrated. The high-q range (C) shows a more broadly distributed intensity pattern, with higher intensity regions extending over larger areas. Although this peak is also present in CTMP-containing samples, it is much less dominant than in SW-rich materials; therefore, variations in this range are interpreted mainly as reflecting ordered fibrillar domains, with stronger contributions from SW-rich regions. Moreover, the presence of directionally elongated or anisotropic intensity features in the maps suggests that the underlying fibre orientation also influences the scattering response. This observation motivates the directional (azimuthal) analysis presented in the following section.

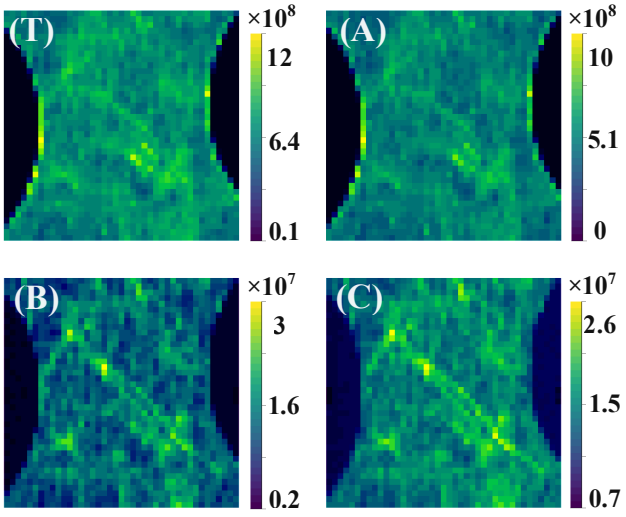

Fig. 4 SAXS intensity maps from the non-deformed scan of the middle ply, with the vertical direction corresponding to the machine direction (MD). (T) Total integrated q-range; (A) low-q range 0.01–0.03Å^{-1}; (B) intermediate-q range 0.04–0.09Å^{-1}; (C) high-q range 0.10–0.25Å^{-1}. Scale bars show the integrated scattering intensity in arbitrary units (a.u.)

In-situ tensile testing with SAXS mapping

A custom-built uniaxial tensile loading device was mounted on the beamline's rotation/translation stage to enable synchronised mechanical loading and data acquisition. The device was originally designed for in-situ μXRT measurements (see Johansson et al. 2021) and was adapted for optimised SAXS measurements by incorporating windows along the beam direction. Samples were mounted with a 10 mm gauge length between the grips of the tensile stage (see Fig. 1). The grip design is based on that described by (Tryding et al. 2017) and consists of a cylindrical element (3 mm in diameter) and a flat surface between which the sample is clamped. More detail on the grips can be found in Johansson et al. (2021). Single-ply sheets (top, middle and bottom) and three-ply boards were tested under in-situ tensile loading in both the MD and CD orientations.

Tensile loading was applied in a stepwise manner using fixed displacement increments for each test, typically in the range 0.07–0.1 mm. The exact step size varied depending on sample type and tensile strength of each specimen, as determined from tensile tests conducted prior to the SAXS experiments. In total, five to six load steps were recorded for each sample, extending up to 0.6 mm total displacement and well beyond the point of failure for all tested specimens.

SAXS mapping for samples subjected to mechanical loading was performed using a similar method as in the non-deformed case. The same $4 \times 4\,\mathrm{mm}^2$ region was scanned using a 40×41 mesh grid, but with the mapping being repeated at several predefined loading steps for each sample, enabling investigation of structural evolution during tensile deformation.

As in the non-deformed condition, the scattering intensity at each mesh point was quantified by integrating the SAXS signal over the predefined q-ranges A, B, C and T. To allow meaningful visual comparison across different load steps, a common colour scale was defined for each q-range using the minimum and maximum intensity values across all loading steps of a given sample. The same colour scale was applied to all corresponding maps, ensuring that changes in scattering intensity observed in the colour maps reflect true structural evolution rather than changes in contrast range between steps. The SAXS intensity maps were constructed using

the same procedure as in the non-deformed-state analysis, enabling direct comparison between loading steps and capturing the spatial evolution of nanostructural features during deformation.

Azimuthal Sectioning and Directional SAXS Mapping

The directional SAXS analysis is based on the scattering geometry of fibrillar structures with a high aspect ratio, which can be approximated as long cylinders. Scattering from such structures is concentrated in directions perpendicular to the fibril axis (Feigin and Svergun 1987; Glatter and Kratky 1982; Guinier et al. 1955). Consequently, the azimuthal distribution of the SAXS intensity provides information about the orientation of fibrillar structures within the sample.

To further investigate anisotropic features and directional variations in nanostructural organisation, the SAXS frames were analysed using azimuthal sectioning. In this approach, the 2D scattering data from each mesh point were segmented into defined azimuthal angle (ϕ) sectors corresponding to four principal directions: vertical ($\pm15°$ around 90° and 270°), horizontal ($\pm15°$ around 0° and 180°) and two diagonals ($\pm15°$ around 45° and 225°, and $\pm15°$ around 135° and 315°). These ϕ-ranges were chosen to capture scattering along and across the primary fibre orientations expected in the paperboard microstructure. A fifth sector covering the full azimuthal range (0°–360°) was also included for reference.

For each direction and mesh point, the scattering intensity was integrated over both the selected azimuthal angles and specific q-ranges defined previously based on the fitted SAXS peaks (Fig. 3). This directional filtering allowed the total intensity within a given q-range to be quantified separately for each direction, thereby revealing orientation-dependent features that may otherwise be masked by full-circle averaging.

To allow consistent visual comparison, a common colour scale was defined within each q-range and ϕ sector using the minimum and maximum intensity values across the corresponding set of maps. The direction-resolved intensity values were then reconstructed into 2D maps using the same procedure described in the previous section. This approach enables local variations in fibre orientation and structural features to be compared consistently across the maps.

X-ray microtomography measurements and data processing

μXRT was performed using a Zeiss Xradia Versa XRM520 system at the 4D Imaging Lab, Lund University, Sweden. After completion of the SAXS experiments, the samples were scanned to evaluate internal structural features and deformation features induced by tensile loading. A total of 3201 radiographs of 2048×2048 pixels were collected over a 360° rotation using an X-ray tube voltage of 80 kV, power of 7 W and an exposure time of 1.2 seconds per projection.

The imaging geometry, in combination with 4× optical magnification, yielded voxels of width 1.75 μm after reconstruction. The tomographic reconstruction was performed with the Zeiss Xradia Reconstructor software with centre-of-rotation correction and a standard beam hardening correction. The resulting image stacks were cropped to a region of interest (ROI) around the notch area to focus on zones of deformation and failure.

Both non-deformed and tensile-loaded samples previously characterised via SAXS were scanned with μXRT, enabling post-mortem 3D analysis of internal structure. Visualisation and post-processing of the μXRT data were performed using Dragonfly software (Comet Technologies Canada Inc. 2025). For selected samples, fibre segmentation was carried out using a combination of global thresholding and the multi-slice brush tool in Dragonfly. This tool allowed grey-level-based segmentation to be propagated efficiently across slices, enabling isolation of fibre structures for further qualitative and quantitative assessment.

Results & Discussion

Scattering features of different samples

The azimuthally averaged SAXS intensity profiles $I(q)$ in Fig. 3, together with their corresponding model fits, reveal several key features associated with distinct structural regimes within the fibre networks (the plotted and fitted profiles represent averages over central regions of each sample). The interpretation of these data in terms of the average structure of each material type is discussed in the following.

At low-q values, corresponding to q-range A (q = 0.01–0.03 Å^{-1}), all samples exhibited a characteristic decay in scattering intensity that follows a power-law behaviour, $I(q) = Pq^{-n}$, with $n \approx 3.7$ and P depending on the material as given in Table 2. This behaviour is approximately Porod-like scattering and indicates that the SAXS signal in this regime is dominated by nanoscale interfaces and density heterogeneities within

the fibre network such as fibre-wall pores and voids and interfaces between the cellulose-rich fibre wall and air-filled regions. Given that the fibre diameter, on the order of tens of micrometres, is significantly larger than the SAXS length scale accessible at $q_{\min} \approx 0.01\,\text{Å}^{-1}$ (corresponding to structural features on the order of d $\sim 60\,\text{nm}$, based on the inverse relationship $d = 2\pi/q$), the observed power-law decay is attributed primarily to fibre-surface morphology and elongated nanoscale pores and voids aligned parallel to the fibre axis (Glatter and Kratky 1982; Jakob et al. 1996; Andersson et al. 2000).

In the high-q range, corresponding to q-range C ($q = 0.1$–$0.25\,\text{Å}^{-1}$), all samples exhibited a pronounced scattering peak centred near $0.1\,\text{Å}^{-1}$, corresponding to a characteristic correlation length of approximately 6 nm. This feature has been observed in most previous studies on cellulose-based materials using SAXS and has commonly been associated with the lateral packing distance or correlation distance of cellulose microfibrils within the fibre wall matrix (Andersson et al. 2000; Kennedy et al. 2007; Fernandes et al. 2011; Leppänen et al. 2009). The position of this peak is approximately constant across the sample series in this study, indicating that the characteristic fibrillar spacing was similar in both CTMP- and SW-containing materials. However, the intensity of the peak varied strongly between samples, with SW-rich samples showing a more pronounced q-range C peak than CTMP-rich samples.

In the intermediate-q range, corresponding to q-range B ($q = 0.04$–$0.09\,\text{Å}^{-1}$), a broad scattering feature centred around $0.04\,\text{Å}^{-1}$ was observed only in samples containing CTMP fibres. The corresponding real-space length scale, estimated as $2\pi/q$, is approximately 15–16 nm. Rather than assigning this feature directly to a single structural element, it is more appropriate to interpret it as evidence of an additional level of nanoscale heterogeneity in the CTMP-containing materials. Lignified softwood cell walls can be described as containing at least three distinct phases: crystalline cellulose fibrils, matrix polymers such as lignin and hemicelluloses and a third phase corresponding to voids in dry samples (Jungnikl et al. 2008). CTMP fibres are produced under milder chemical conditions than kraft fibres and retain a larger fraction of the original lignin- and hemicellulose-rich matrix (Lahtinen et al. 2014; Brännvall 2009). Therefore, the additional broad feature in q-range B is interpreted as being associated with the retained matrix polymers.

Taken together, the observed differences in the SAXS response suggest that different pulping processes affect the fibre wall nanostructure in different ways. Even mild chemical delignification will modify lignin, polysaccharide and cellulose structures and may, therefore, change

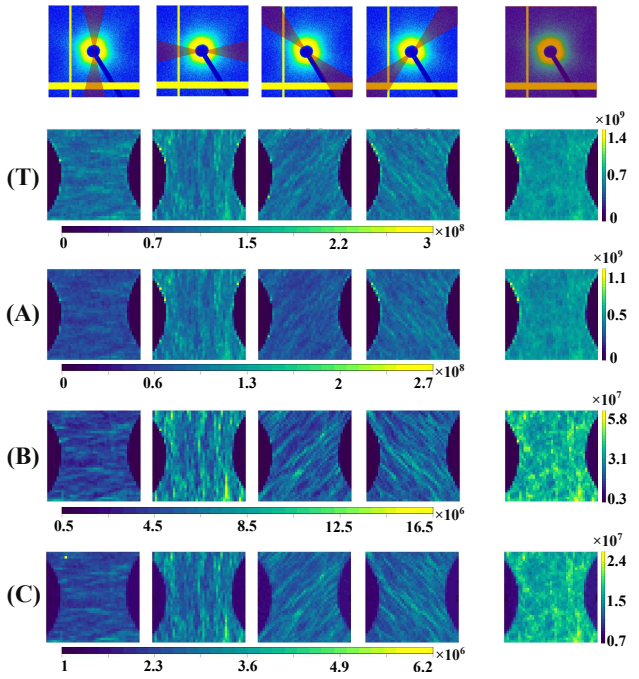

Fig. 5 SAXS intensity maps acquired before loading for the middle ply in the machine direction (MD), resolved by azimuthal sector and q-range. Rows represent different q-ranges: (T) total integrated q-range; (A) 0.01–0.03 Å^{-1}; (B) 0.04–0.09 Å^{-1}; (C) 0.10–0.25 Å^{-1}. Columns correspond to azimuthal sectors: vertical, horizontal, diagonal (top-left to bottom-right), diagonal (top-right to bottom-left) and total azimuthal integration (0°–360°). For each row and each total-ϕ map, the colour scale was defined using the minimum and maximum intensity values across the corresponding set of maps.

the organisation of the fibre wall (Brännvall et al. 2021; Iglesias et al. 2020; Esteves et al. 2023). Thus, the differences between CTMP and SW samples can be viewed as differences in how the original fibrillar and matrix organisation has been preserved or modified during pulping. In chemically extracted or delignified softwood (i.e., Kraft pulp), removal of matrix polymers can make the cell wall system closer to a two-phase case, where the dominant SAXS contrast arises mainly between cellulose fibrils and the spacing between them (Jungnikl et al. 2008; Brännvall 2009; Lahtinen et al. 2014). In contrast, with CTMP processing, the cell walls retain more of the original lignified cell wall composition and are, therefore, better described as a three-phase system. This interpretation explains why the q-range C peak is more dominant in SW-rich samples, while CTMP-containing samples exhibit the additional feature in the B q-range.

Azimuthal Sectioning and orientation analysis

To analyse fibril orientations in the studied paperboard samples, azimuthal sectioning was applied, as described

earlier. As the greatest scattering from the microfibrils is expected to be perpendicular to their axis, higher intensities mapped along a detector direction reflect fibrils that lie around the sample plane rotated 90° from that direction. The sector-resolved maps in Fig. 5 show that azimuthal sectioning of the scattering pattern makes it possible to separate scattering contributions from fibrils oriented in different directions. Since the cellulose microfibrils are related to the fibre axis through the microfibril angle (Donaldson 2008), these directional scattering features can be used as an indirect indication of the spatial distribution of fibres with different orientations. Combining azimuthal sectoring with the selected q-ranges therefore provides a way to investigate how orientation-dependent structural features are distributed within the fibre network. This is important for the subsequent loading analysis, where changes in scattering intensity can be evaluated as a function of both orientation and q-range to assess how fibre alignment influences the mechanical response.

Spatial evolution of SAXS signals and nanostructure during loading

Figure 6 shows the force–displacement response of middle ply specimens loaded in MD and CD, with markers indicating the loading steps at which SAXS mapping was performed. These curves provide the mechanical context for interpreting the evolution of the SAXS intensity maps presented below. The different force levels and failure evolution observed for MD and CD loading indicate anisotropic mechanical behaviour at the macro scale and, thus, it is interesting to explore how this manifests on the smaller scales.

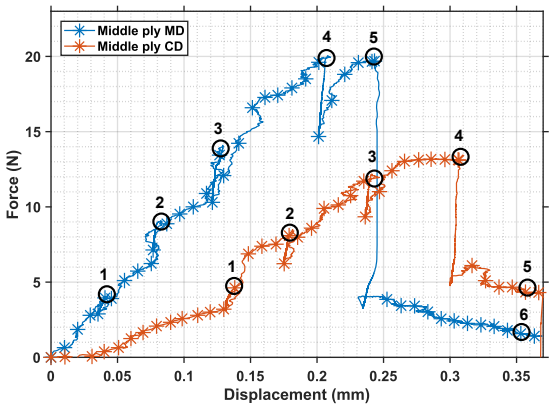

Fig. 6 Force–displacement response for middle-ply tensile tests in the MD and CD directions. The experimental response is shown by the continuous curves, with star markers indicating selected data points. The numbered markers identify the loading steps at which SAXS mapping was performed.

SAXS intensity maps of the middle ply board loaded in-situ along the CD direction, integrated over the full azimuthal range, are shown in Fig. 7 for successive loading steps. The maps reveal gradual and spatially heterogeneous changes in scattering intensity as deformation progresses. At early loading steps, only subtle variations are observed, primarily within the central notch region. With increasing axial deformation, the low-q maps, corresponding to q-range A (Fig. 7), develop progressively elevated intensity across the notch region, forming a broad transverse zone that becomes more pronounced at later loading stages. Since q-range A is dominated by power-law scattering, this behaviour suggests the progressive formation of new internal interfaces and voids associated with damage development, including fibre-aligned fracture surfaces and fibre-aligned separation within the fibre network. In contrast, the CTMP-related q-range (q-range B) remains comparatively stable over most of the loading sequence, with only localised intensity variations appearing at higher deformation levels. Changes in the SW-related q-range (q-range C) are more limited and emerge only close to the maximum load (red marker in Fig. 7). In this q-range, narrow regions of reduced intensity become visible within the notch zone, suggesting a local reduction in the amount of densely packed fibrillar material contributing to the scattering signal. Following peak load, the localised brightening in q-range A becomes more pronounced, while the reduced intensity in q-range C develops further within the same fracture region, consistent with opening of the fibre network and progressive material separation during fracture.

For all investigated samples, single-ply sheets as well as the three-ply board, under both MD and CD loading, qualitatively similar behaviour was observed in the low-q power-law response (q-range A), where localised brightening progressively developed within the notch and fracture regions. Figure 8 summarises the final loading step for each sample type. Although the spatial distribution and geometry of these regions differ between MD and CD loading, consistent with the different fibre orientations relative to the applied load, the same overall damage signature was observed across all sample configurations. To quantify the localised brightening trend, the integrated intensity in q-range A was evaluated for each loading step by summing the intensity over all scan positions and azimuthal angles and normalising by the initial non-loaded step for each sample (see Fig. 9). As the in-situ loading involved different numbers of loading steps and different final displacements for each sample, the x-axis in Fig. 9 was expressed as deformation progress, calculated as:

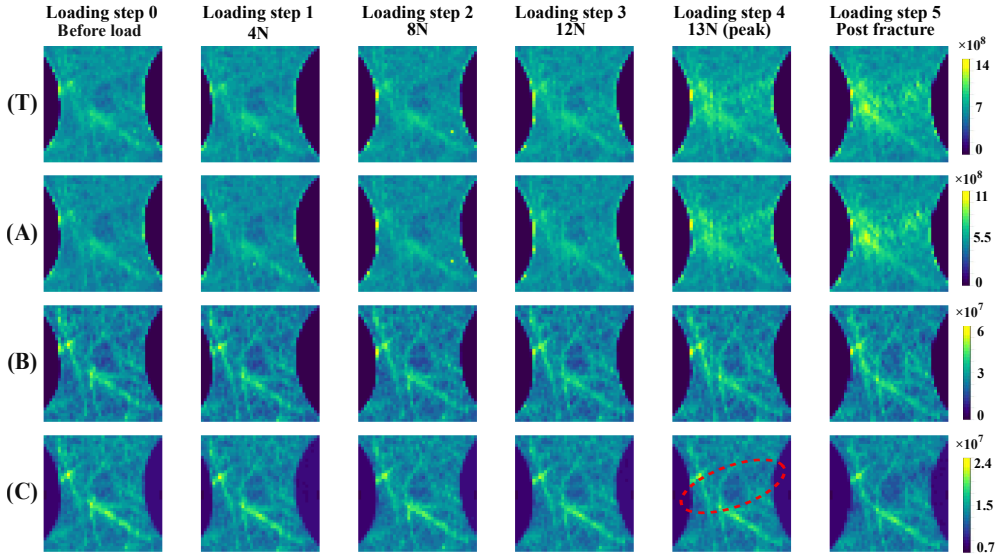

Fig. 7 SAXS intensity maps of the middle ply sample loaded in-situ in the CD across incremental tensile loading steps. Rows represent different q-ranges: (T) total integrated q-range; (A) 0.01–0.03 Å^{-1}; (B) 0.04–0.09 Å^{-1}; (C) 0.10–0.25 Å^{-1}. Columns correspond to incremental loading steps from non-deformed to post-fracture. Each row shares a common colour scale, defined using the minimum and maximum intensity values across all loading steps within the same q-range to highlight relative intensity evolution.

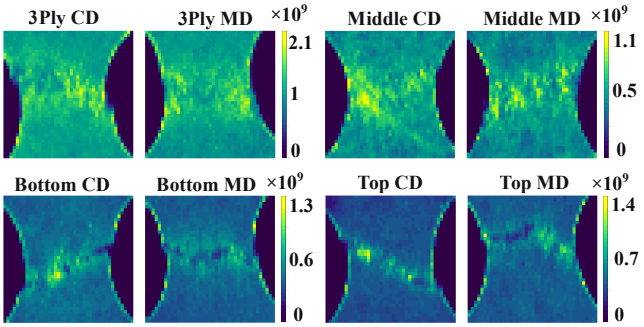

Fig. 8 Low-q SAXS intensity maps (q-range A, power-law dominated scattering) at the final loading step for all investigated sample configurations under MD and CD loading. Localised brightening is consistently observed within the notch and fracture regions.

$$\text{Deformation progress } (\%) = \frac{d_i}{d_{\text{final}}} \times 100, \tag{4}$$

where d_i is the displacement at loading step i and d_{final} is the final displacement of the corresponding sample. Each marker in Fig. 9 represents one SAXS measurement point acquired at a specific loading step. For all investigated samples, the Region A intensity increased with loading. In most cases, the maximum intensity occurred at the failure step, while the subsequent post-failure scan shows a slight decrease. This suggests that the formation of new internal interfaces and voids dominates the low-q scattering response up to failure, whereas after fracture, continued opening and separation of the fibre network may reduce the amount of material contributing within the scanned volume.

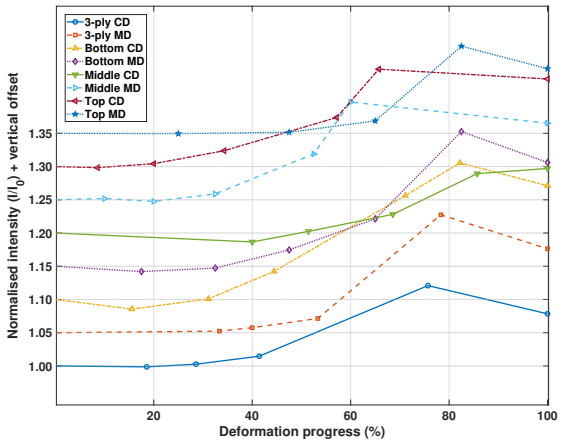

Fig. 9 Evolution of the integrated SAXS intensity in q-range A (q = 0.01–0.03 Å^{-1}) with deformation progress for all sample configurations. Intensities were summed over all scan positions and azimuthal angles and normalised by the initial non-loaded step (I/I_0). Each marker represents one SAXS loading step, with deformation progress calculated as the displacement at each loading step normalised by the final displacement of the corresponding sample. Curves are vertically offset in increments of 0.05 for clarity.

Comparison between SAXS mapping and μXRT

To relate spatial variations in the SAXS intensity maps to the underlying fibre-network structure, SAXS mapping results were correlated with μXRT for the investigated samples, both prior to loading and after tensile deformation. This comparison was performed for single-ply sheets and three-ply boards under both loading orientations, enabling nanoscale scattering features to be related to the corresponding fibre-network architecture resolved in 3D.

Post-mortem μXRT images of the middle-ply sample loaded in the cross direction (CD) are shown in Fig. 10. The fracture zone is visible as an extended, spatially localised region of internal damage, with fibre rupture, pronounced internal separation and opening of the fibre network. The spatial extent and orientation of this fracture corridor correspond well with the regions of enhanced SAXS intensity observed in q-range A.

Despite the fundamental differences in contrast mechanism and spatial resolution between SAXS and μXRT, a clear spatial correspondence can be observed between features in the SAXS maps and the fibre-network morphology resolved by μXRT. Elongated intensity patterns and local contrast variations in the SAXS maps align with fibre-rich regions, fibre bundles and network features visible in the tomographic reconstructions. This correspondence supports the interpretation that variations in scattering intensity, particularly in the SW-related peak q-range (Range C), reflect the local organisation and continuity of fibres. The ability to trace fibre-scale features through SAXS arises from the continuity of cellulose microfibril packing along fibre-aligned structures, which produces a spatially coherent scattering response along the fibre axis.

The localised regions of reduced SAXS intensity in q-range C coincide with areas of fibre rupture and network

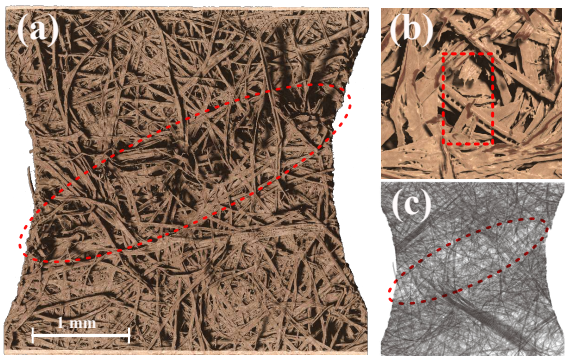

Fig. 10 Post-loading μXRT of the middle ply sample loaded in CD. (a) standard 3D rendering of the full sample, with the fracture zone clearly visible; (b) Focused view showing a fibre rupture within the fracture zone; (c) low-opacity rendering highlighting the extent of the internal fracture.

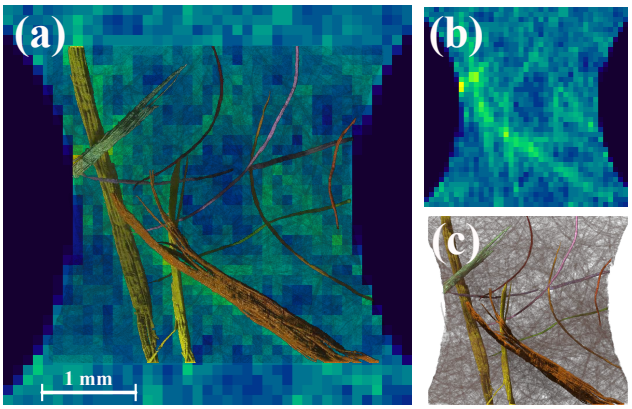

Fig. 11 Comparison between SAXS mapping and post-loading μXRT for the middle ply sample in the cross direction (CD). (a) overlay of the 3D rendering with the SAXS intensity map showing spatial correspondence between nanostructural and microstructural features; (b) SAXS intensity map integrated over q-range C; (c) partially segmented fibre network highlighting internal architecture.

separation observed in the μXRT volumes (see Fig. 11). Similar correlations between SAXS intensity patterns and fibre-network features were observed across the full sample set and loading conditions, confirming that the observed correspondence is not specific to a single ply or loading case.

Spatial evolution of direction-dependent SAXS signals

Azimuthal sectioning of the SAXS data provides additional insight into the directional character of the nanostructural changes observed during tensile loading. Figure 12 shows the azimuthally resolved SAXS intensity maps for the middle ply loaded in the machine direction (MD) at the final loading step. Corresponding maps for other loading steps, loading directions and sample configurations are provided in the supplementary material. Comparison with the corresponding maps acquired before loading in Fig. 5 helps distinguish deformation-induced changes from the initial structural anisotropy of the fibre network.

In the MD-loaded middle ply, the azimuthal sector corresponding to scattering perpendicular to the fibre axis (horizontal orientation sector) exhibits the most pronounced intensity variations within the notch region at the final loading stage. In particular, vertically aligned corridors of increased intensity develop across the fracture zone, extending approximately along the loading direction. These features are most clearly visible in the low-q response and suggest that nanostructural damage preferentially evolves along fibre-aligned paths within the network. Relative to the initial maps acquired before loading, these localised intensity corridors become sub-

stantially more pronounced during loading, indicating that they are associated with deformation and fracture rather than solely with the original fibre structure. The vertical orientation sector exhibits regions of elevated intensity outside the main fracture zone, some of which are already visible in the corresponding non-deformed condition maps. This suggests that part of the directional scattering contrast reflects the initial structural organisation of the fibre network, while the additional localised brightening observed during loading is associated with deformation-induced damage. Comparison with the full loading sequence (see supplementary material) indicates that the directional intensity variations become increasingly localised with increasing axial load, particularly during the final loading steps near peak load and fracture (Fig. 6).

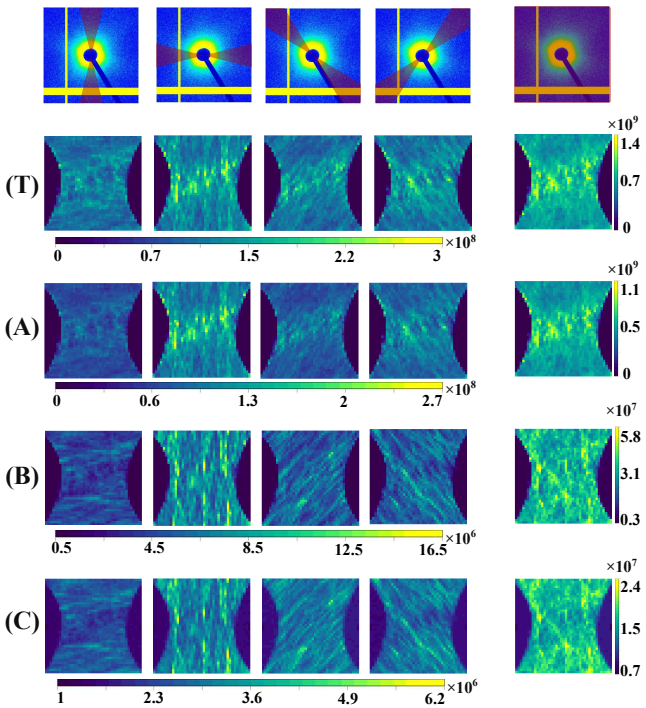

Fig. 12 Azimuthally resolved SAXS intensity maps of the middle ply loaded in the machine direction (MD) at the final loading step. The top row indicates the azimuthal sectors used for directional integration in each column. Rows represent different q-ranges: (T) total integrated q-range; (A) 0.01–0.03 $Å^{-1}$; (B) 0.04–0.09 $Å^{-1}$; and (C) 0.10–0.25 $Å^{-1}$. The colour scale represents scattering intensity. Additional loading steps and sample configurations are provided in the supplementary material.

For the middle ply loaded in CD, as well as for the top, bottom and three-ply boards under both loading directions, azimuthally resolved maps show qualitatively similar behaviour but with different spatial organisation and different orientation sectors exhibiting the most pronounced intensity variations, reflecting the different fibre orientations relative to the applied load. These results are included in the supplementary material for comparison. Overall, the azimuthally resolved SAXS maps indicate that while nanostructural changes occur across multiple scattering directions, their spatial distribution and relative magnitude depend on the loading direction and fibre alignment.

Conclusion

This study combined 2D scanning SAXS, μXRT and tensile testing to investigate the nanostructure and deformation mechanisms in paperboard. The sample set included single-ply sheets, three-ply boards and isotropic reference sheets, enabling comparison between fibre type, ply structure and loading direction. In the first part of the work, both single-ply and three-ply configurations were studied before tensile loading to characterise their internal fibre architecture using 2D SAXS mapping and μXRT. In the second part, a separate set of single-ply and three-ply samples were subjected to in-situ stepwise uniaxial tensile loading, followed by post-mortem μXRT.

1D integrated SAXS profiles revealed nanostructural differences between CTMP- and SW-rich materials. For the SW fibres, the scattering features are consistent with those described in previously published works, but an additional lower-q peak contribution is observed in CTMP-containing samples, indicating different structures in the fibre walls. CTMP processing leads to fibres that have retained more of the original lignified cell wall composition and are, therefore, better described as a three-phase system consisting of cellulose fibrils, matrix polymers and voids. In contrast, kraft-pulped SW fibres show a stronger high-q response associated with ordered fibrillar domains, no peak at lower q, and an overall scattering behaviour that is closer to a two-phase fibril–spacing system. Spatial SAXS mapping further revealed fibre-aligned scattering features that correlated with structures observed by μXRT. The CTMP-related intensity in the SAXS maps was more localised, whereas the SW-related response was more broadly distributed across the fibre network, as this peak is seen in both the CTMP and SW fibres. Azimuthal SAXS analysis additionally showed that these scattering features were directionally dependent, reflecting the underlying fibre and fibril orientations.

SAXS analysis during stepwise in-situ tensile loading revealed a clear brightening in the power-law q-range of the scattering signal within developing failure zones. The integrated intensity in q-range A generally increased with loading and reached a maximum at or near the

failure step (Fig. 9). The power-law scattering that dominates in this q-range is known to originate from sharp interfaces in heterogeneous materials (Jakob et al. 1996). This suggests that the increase in scattering intensity at this scale range observed during the tensile loading in this work is are most plausibly associated with the formation of pores, cavities and internal interfaces within fibre walls and at fibre-network interfaces. The observed brightening is, therefore, interpreted as an indicator of structural damage at sub-micrometre length scales; this is one of the key findings of this work. This damage may arise from several concurrent deformation processes, including fibre-wall fibrillation, internal separation, fibre–fibre debonding and, in multi-ply samples, ply-level delamination. Previous observations of pronounced thickening near peak load of samples under tensile loading (Johansson et al. 2021) are consistent with the current observations and the interpretation of damage formation through fibre-fibre bond breakage and delamination, but the SAXS suggests that there is also intra-fibre damage. These processes are analogous to the mechanical failure of a rope, where stretching leads to separation into individual strands and an overall expansion of the structure as internal cohesion is lost. In paperboard, a similar process likely occurs through progressive fibre-wall damage and network separation; however, direct verification of this mechanism would require further studies on individual fibres and fibre bonds.

In several samples, the post-failure SAXS scan showed a slight decrease of the power-law intensity relative to pre-failure (Fig. 9), which is likely related to continued opening of the fibre network that reduces the amount of material contributing to the scattering within the scanned volume, partly counteracting the scattering contribution from newly formed interfaces.

In addition to the brightening observed in the power-law q-range, a distinct crack-like darkening of the SAXS signal was detected in samples containing both SW and CTMP fibres, particularly within the middle-ply and three-ply configurations. This effect was more pronounced in the q-range associated with SW fibres than in the CTMP-related range, suggesting that SW-rich regions may be more strongly affected by local fibre rupture or loss of ordered fibrillar material within the fracture zone, while CTMP-rich regions may undergo more gradual debonding and internal separation. In the three-ply configuration, this behaviour is consistent with a possible layered failure process, where damage develops first in the CTMP-containing middle ply and subsequently involves the SW-dominated outer plies.

The increase in SAXS intensity in the power-law q-range provides evidence for the formation of additional internal interfaces and voids during tensile deformation. This response was observed as localised brightening in q-range A and is consistent with observations from the post-loading μXRT, which revealed internal separation, opening of the fibre network and fibre rupture within the fracture zone. These findings indicate that the tensile failure of paperboard is a progressive, multiscale process involving fibre-network separation, fibre-wall damage and fibre rupture, with the relative importance of these mechanisms governed by fibre type, ply structure and loading direction. Future models for advanced simulation of paperboard deformation should endeavour to capture these processes.

Acknowledgements

The authors gratefully acknowledge Tetra Pak AB for financial support of this project. Billerud AB is acknowledged for custom manufacturing and supplying the paperboard samples used in this study. We acknowledge the MAX IV Laboratory for beamtime on the ForMAX beamline under proposal number 20240550. Research conducted at MAX IV, a Swedish national user facility, is supported by Vetenskapsrådet (Swedish Research Council, VR) under contract 2018-07152, Vinnova (Swedish Governmental Agency for Innovation Systems) under contract 2018-04969 and Formas under contract 2019-02496. The authors also acknowledge the use of Dragonfly Image Processing and Data Analysis Software for visualisation and analysis of the X-ray tomography data.

References

Andersson S, Serimaa R, Torkkeli M, Paakkari T, Saranpää P, Pesonen E (2000) Microfibril angle of norway spruce [picea abies (l.) karst.] compression wood: comparison of measuring techniques. Journal of Wood Science 46(5):343–349, https://doi.org/10.1007/BF00776394

Auernhammer J, Langhans M, Schäfer JL, Keil T, Meckel T, Biesalski M, Stark RW (2022) Nanomechanical subsurface characterisation of cellulosic fibres. SN Applied Sciences 4(6):160, https://doi.org/10.1007/s42452-022-05017-9

Barnett JR, Bonham VA (2004) Cellulose microfibril angle in the cell wall of wood fibres. Biological reviews 79(2):461–472, https://doi.org/10.1017/S1464793103006377

Brännvall E (2009) 1. overview of pulp and paper processes. In: Ek M, Gellerstedt G, Henriksson G (eds) Volume 2 Pulping Chemistry and Technology,

De Gruyter, Berlin, New York, pp 1–12, https://doi.org/10.1515/9783110213423.1

Brännvall E, Larsson PT, Stevanic JS (2021) Changes in the cellulose fiber wall supramolecular structure during the initial stages of chemical treatments of wood evaluated by nmr and x-ray scattering. Cellulose 28(7):3951–3965, https://doi.org/10.1007/s10570-021-03790-1

Cave I (1997) Theory of x-ray measurement of microfibril angle in wood: Part 1. the condition for reflection x-ray diffraction by materials with fibre type symmetry. Wood science and technology 31(3):143–152, https://doi.org/10.1007/BF00705881

Comet Technologies Canada Inc (2025) Dragonfly 3D World. URL https://dragonfly.comet.tech/, version 2025.1, computer software

Dias PA, Rodrigues RJ, Reis MS (2023) Fast characterization of in-plane fiber orientation at the surface of paper sheets through image analysis. Chemometrics and Intelligent Laboratory Systems 234:104761, https://doi.org/10.1016/j.chemolab.2023.104761

Donaldson L (2008) Microfibril angle: measurement, variation and relationships–a review. IAWA Journal 29(4):345–386, https://doi.org/10.1163/22941932-90000192

El-Hosseiny F, Page D (1975) The mechanical properties of single wood pulp fibres: theories of strength. Fibre Science and Technology 8(1):21–31, https://doi.org/10.1016/0015-0568(75)90012-3

Esteves CV, Brännvall E, Stevanic JS, Larsson PT (2023) Pulp delignification and refining: Impact on the supramolecular structure of softwood fibers. Cellulose 30(16):10453–10468, https://doi.org/10.1007/s10570-023-05490-4

Feigin LA, Svergun DI (1987) Structure Analysis by Small-Angle X-Ray and Neutron Scattering. Springer, New York, https://doi.org/10.1007/978-1-4757-6624-0

Fellers C (2009) 1. the structure of paper and its modelling. In: Ek M, Gellerstedt G, Henriksson G (eds) Volume 4 Paper Products Physics and Technology, De Gruyter, Berlin, New York, pp 1–24, https://doi.org/10.1515/9783110213461.1

Fernandes AN, Thomas LH, Altaner CM, Callow P, Forsyth VT, Apperley DC, Kennedy CJ, Jarvis MC (2011) Nanostructure of cellulose microfibrils in spruce wood. Proceedings of the National Academy of Sciences 108(47):E1195–E1203, https://doi.org/10.1073/pnas.1108942108

Fratzl P, Jakob H, Rinnerthaler S, Roschger P, Klaushofer K (1997) Position-resolved small-angle x-ray scattering of complex biological materials. Journal of Applied Crystallography 30(5):765–769, https://doi.org/10.1107/S0021889897001775

Glatter O, Kratky O (eds) (1982) Small Angle X-ray Scattering. Academic Press, London

Groom LH, Mott L, Shaler S (2002) Mechanical properties of individual southern pine fibers. part i. determination and variability of stress-strain curves with respect to tree height and juvenility. Wood and Fiber Science 34(1):14–27

Guinier A, Fournet G, Walker CB, Yudowitch KL (1955) Small-angle Scattering of X-rays. Wiley, New York

Hubbe MA (2014) Prospects for maintaining strength of paper and paperboard products while using less forest resources: A review. BioResources 9(1):1634–1763, https://doi.org/10.15376/biores.9.1.1634-1763

Iglesias MC, Gomez-Maldonado D, Via BK, Jiang Z, Peresin MS (2020) Pulping processes and their effects on cellulose fibers and nanofibrillated cellulose properties: A review. Forest Products Journal 70(1):10–21, https://doi.org/10.13073/FPJ-D-19-00038

Jakob H, Fratzl P, Tschegg S (1994) Size and arrangement of elementary cellulose fibrils in wood cells: a small-angle x-ray scattering study of picea abies. Journal of Structural Biology 113(1):13–22, https://doi.org/10.1006/jsbi.1994.1028

Jakob H, Fengel D, Tschegg S, Fratzl P (1995) The elementary cellulose fibril in picea abies: comparison of transmission electron microscopy, small-angle x-ray scattering, and wide-angle x-ray scattering results. Macromolecules 28(26):8782–8787, https://doi.org/10.1021/ma00130a010

Jakob H, Tschegg S, Fratzl P (1996) Hydration dependence of the wood-cell wall structure in picea abies. a small-angle x-ray scattering study. Macromolecules 29(26):8435–8440, https://doi.org/10.1021/ma9605661

Jensen AB, Christensen TEK, Weninger C, Birkedal H (2022) Very large-scale diffraction investigations enabled by a matrix-multiplication facilitated radial and azimuthal integration algorithm: Matfraia. Journal of Synchrotron Radiation 29(6):1420–1428, https://doi.org/10.1107/S1600577522008232

Johansson S, Engqvist J, Tryding J, Hall S (2021) 3d strain field evolution and failure mechanisms in anisotropic paperboard. Experimental Mechanics 61(3):581–608, https://doi.org/10.1007/s11340-020-00681-7

Jungnikl K, Paris O, Fratzl P, Burgert I (2008) The implication of chemical extraction treatments on the cell wall nanostructure of softwood. Cellulose 15(3):407–418, https://doi.org/10.1007/s10570-007-9181-5

Kennedy CJ, Cameron GJ, Šturcová A, Apperley DC, Altaner C, Wess TJ, Jarvis MC (2007) Microfibril diameter in celery collenchyma cellulose: X-ray scattering and nmr evidence. Cellulose 14(3):235–246, https://doi.org/10.1007/s10570-007-9116-1

Kloppenburg G, Li X, Dinkelmann A, Finckh H, Neumann J, Simon JW (2024) Functional description of fiber orientation in paperboard based on orientation tensors resulting from μ-ct scans. Cellulose 31(13):7865–7893, https://doi.org/10.1007/s10570-024-06094-2

Kompella MK, Lambros J (2002) Micromechanical characterization of cellulose fibers. Polymer Testing 21(5):523–530, https://doi.org/10.1016/S0142-9418(01)00119-2

Lahtinen P, Liukkonen S, Pere J, Sneck A, Kangas H (2014) A comparative study of fibrillated fibers from different mechanical and chemical pulps. BioResources 9(2):2115–2127, https://doi.org/10.15376/biores.9.2.2115-2127

Larsson PT, Stevanic-Srndovic J, Roth SV, Söderberg D (2022) Interpreting saxs data recorded on cellulose rich pulps. Cellulose 29(1):117–131, https://doi.org/10.1007/s10570-021-04291-x

Leppänen K, Andersson S, Torkkeli M, Knaapila M, Kotelnikova N, Serimaa R (2009) Structure of cellulose and microcrystalline cellulose from various wood species, cotton and flax studied by x-ray scattering. Cellulose 16(6):999–1015, https://doi.org/10.1007/s10570-009-9298-9

Lichtenegger H, Reiterer A, Stanzl-Tschegg S, Fratzl P (1999) Variation of cellulose microfibril angles in softwoods and hardwoods—a possible strategy of mechanical optimization. Journal of structural biology 128(3):257–269, https://doi.org/10.1006/jsbi.1999.4194

Nygård K, McDonald S, González J, Haghighat V, Appel C, Larsson E, Ghanbari R, Viljanen M, Silva J, Malki S, et al. (2024) Formax–a beamline for multiscale and multimodal structural characterization of hierarchical materials. Journal of Synchrotron Radiation 31(2):363–377, https://doi.org/10.1107/S1600577524001048

Page DH, El-Hosseiny F, Winkler K, Lancaster APS (1977) Elastic modulus of single wood pulp fibers. TAPPI 60(4):114–117

Reiterer A, Jakob H, Stanzl-Tschegg S, Fratzl P (1998) Spiral angle of elementary cellulose fibrils in cell walls of picea abies determined by small-angle x-ray scattering. Wood Science and Technology 32(5):335–345, https://doi.org/10.1007/BF00702790

Saxe F, Eder M, Benecke G, Aichmayer B, Fratzl P, Burgert I, Rüggeberg M (2014) Measuring the distribution of cellulose microfibril angles in primary cell walls by small angle x-ray scattering. Plant Methods 10(1):25, https://doi.org/10.1186/1746-4811-10-25

The MathWorks Inc (2022) Matlab version: 9.13.0 (r2022b). URL https://www.mathworks.com

Thomas LH, Altaner CM, Forsyth VT, Mossou E, Kennedy CJ, Martel A, Jarvis MC (2021) Nanostructural deformation of high-stiffness spruce wood under tension. Scientific reports 11(1):453, https://doi.org/10.1038/s41598-020-79676-2

Tryding J, Marin G, Nygårds M, Mäkelä P, Ferrari G (2017) Experimental and theoretical analysis of in-plane cohesive testing of paperboard. International Journal of Damage Mechanics 26(6):895–918, https://doi.org/10.1177/1056789516630776

Vainio A, Paulapuro H (2007) Interfiber bonding and fiber segment activation in paper. BioResources 2(3):442–458, https://doi.org/10.15376/biores.2.3.442-458

Virtanen T, Penttilä PA, Maloney TC, Grönqvist S, Kamppuri T, Vehviläinen M, Serimaa R, Maunu SL (2015) Impact of mechanical and enzymatic pretreatments on softwood pulp fiber wall structure studied with nmr spectroscopy and x-ray scattering. Cellulose 22(3):1565–1576, https://doi.org/10.1007/s10570-015-0619-x

Wahlström T (2013) Predictions of MD and CD tensile property profiles. In: I'Anson SJ (ed) Advances in Pulp and Paper Research, Cambridge 2013, FRC, Manchester, pp 673–710, https://doi.org/10.15376/frc.2013.2.673

Wardrop A (1952) The low-angle scattering of x-rays by conifer tracheids. Textile Research Journal 22(4):288–291, https://doi.org/10.1177/004051755202200408

Statements and Declarations

Funding

This work was financially supported by Tetra Pak AB.

Competing interests

The authors have no Competing interests to disclose.

Data availability

The datasets generated and analysed during the current study are available from the corresponding author on reasonable request.

Code availability

Custom Python and MATLAB scripts used for data processing and analysis are available from the corresponding author on reasonable request.

Ethics approval

Not applicable.

Supplementary Files

This is a list of supplementary files associated with this preprint. Click to download.

- supplementarymaterials.zip